Hierarchical MnO$_2$/activated carbon cloth electrode prepared by synchronized electrochemical activation and oxidation for flexible asymmetric supercapacitors

Jie Zhang[a,b], Jiangbo Sun[a], Tofik Ahmed Shifa[c], Di Wang[a], Xiaofeng Wu[a,*], Yanbin Cui[a,b,*]

[a] State Key Laboratory of Multiphase Complex Systems, Institute of Process Engineering, Chinese Academy of Sciences, Beijing 100190, China
[b] Center of Materials Science and Optoelectronics Engineering, University of Chinese Academy of Sciences, Beijing 100049, China
[c] CAS Center for Excellence in Nanoscience, CAS Key Laboratory of Nanosystem and Hierarchical Fabrication, National Center for Nanoscience and Technology, Beijing 100190, China

HIGHLIGHTS

- A novel synthesis of hierarchical MnO$_2$ on activated carbon cloth was designed.
- High-voltage asymmetric supercapacitor delivered impressive volumetric energy density.
- The binder-free H-MnO$_2$/ACC showed high specific capacitance and excellent cycling stability.

ARTICLE INFO

ABSTRACT

Despite appealing supercapacitive properties, the flexible asymmetric supercapacitor devices (FASCs) are still suffering from low mass loading and limited operating voltage, leading to unsatisfactory energy densities. Herein, we introduced a high-voltage anodic electro-deposition process (AED) which is a novel avenue enabling the synthesis of hierarchical MnO$_2$ on activated carbon cloth (H-MnO$_2$/ACC). Interestingly, the concomitant activation of carbon cloth substrate is found to be beneficial to improve the conductivity and hydrophilic nature of our novel electrode. A FASC based on H-MnO$_2$/ACC-300 and reduced carbon cloth (RCC) was assembled using a mixed ionic liquid gel (ionogel) electrolyte. Benefiting from highly conductive paths derived from intimately attached fiber-MnO$_2$ interfaces, hierarchically interpenetrated lamella MnO$_2$ porosity and concentric MnO$_2$ interlayer voids, as well as the merits of ionic liquid, the resultant FASC delivers an output voltage as high as 4 V and an impressive volumetric energy density of 3.82 mWh/cm^3. Furthermore, the optimized H-MnO$_2$/ACC-300 electrode with high mass loading can even retain 94.2% of initial capacitance upon 5000 cycles in 1 M Na$_2$SO$_4$. The unique H-MnO$_2$/ACC can aid in the rational design towards flexible electronic devices with high mass loading and this synthetic strategy opens up enormous possibilities for the fabrication of electrodeposited materials.

1. Introduction

Flexible electronic devices are indispensable parts in modern life, applied widely in mobile electrical products, smart textile and artificial electronic skin, etc. [1–7] In this regard, electrochemical supercapacitors (SCs) have drawn considerable attention and emerged as a promising power source of flexible and lightweight electronic devices owing to their high-power density and long lifetimes [1,3,5]. The ongoing efforts in this scenario, therefore, are intensively focused on electrode design and SC assembly configurations to increase the energy density of flexible supercapacitor (FSC) without sacrificing its intrinsic character [8,9]. Furthermore, solid-state electrolyte instead of liquid one has been used in FSC to avoid electrolyte leaking and minimize the dissolution of the electrode for reliable stability [8,10,11]. Nevertheless, it is more determinative and challenging to fabricate novel electrode materials in order to maximize the energy storage density together with excellent power density, further extending application opportunities [12,13].

A typical flexible supercapacitor electrode is generally constructed on a self-supported substrate such as plastic film, metal foil, and carbon-based material to conduct internal current to the outside supply [14–16]. Among them, carbon cloth (CC), endowing remarkable flexibility and mechanical stability, is a very competent candidate for the binder-free growth of electroactive materials [17–19]. Although CC has desirable flexible features, it still suffers from relatively hydrophobicity and low conductive property, as well as limited electroactive surface area for loading of highly active materials [20,21]. Meanwhile, cycling stability of CC-based electrodes is restricted by the detachment of active materials due to their weak deposit-substrate interaction. To address these problems, pretreatment for the surface of CC fibers is preferentially required so as to improve the adhesion between carbon fiber and pseudocapacitive materials [21–23]. For example, Song *et al.* pretreated CC by electrochemical exfoliation in a 0.5 M KNO_3 electrolyte and then deposited vanadium oxide on exfoliated CC. Amorphous VO_x can, therefore, be firmly anchored on the surface of CC through C-O-V bonding [21]. Similarly, the work of Chien *et al.* who pretreated the surface of CC with atmospheric pressure plasma jet (APPJ) to improve its wettability is another exemplary in modifying the surface [23]. Nevertheless, it is still a substantial room in improving surface chemistry to strengthen the attachment of electroactive materials on electrodes.

With regard to reported active materials anchored on the surface of CC substrate, nanoscale layered manganese dioxide (MnO_2) among transition-metal oxides (TMOs) with rich valence states, stands out as one of the most eye-catching choices for high-performance SC electrodes [1,17,24–28]. Nanostructured MnO_2 can offer plenty of active sites and suitable channels for ion intercalation, and CC simultaneously serves as elastic buffering layers to release the strain within MnO_2 during successive charge-discharge cycling. Unfortunately, the dense MnO_2 films formed through traditional electrodeposition method seriously restrict the utilization of inner parts of MnO_2, resulting in low capacitance and thus hindering their large-scale applications [18,29]. As a result, a high gravimetric capacitance of MnO_2-based hybrid materials are reported when the mass loading is less than $1\,mg\,cm^{-2}$ [30]. Therefore, construction of electrodes with high electrochemical performance and large mass loading is an essential criteria for the designing of MnO_2-based SC. Recently, Nagaraju *et al.* [31] fabricated core-shell-like MnO_2 nanostructures (NSs) decorated MnO_2 hexagonal nanoplate arrays on a CC with a high specific capacitance of 244.54 F/g at 0.5 A/g. Based on Ostwald ripening, Song *et al.* developed a two-step route to prepare a high mass loading MnO_2 electrode with remarkable capacitance of $618\,mF\,cm^{-2}$ at $200\,mV\,s^{-1}$ [18]. But all these methods involve multi-step processes which are costly, complicated and time-consuming. Thus, a straightforward and cost-effective strategy to simultaneously improve the mass loading and potential performance of electrode is urgently desired.

Herein, we synthesized hierarchical MnO_2 (H-MnO_2) nanostructures by a facile one-step anodic electro-deposition (AED) process. During this AED process, the activation of CC and in-situ growth of active material can occur concurrently. Different from the reported anodic and/or cathodic electro-deposition (ED) of MnO_2 [29,31,32], usually producing the uncontrollable MnO_2 polymorphs and poor attachment on substrates, high-concentration Na_2SO_4 electrolyte was employed in our developed anodic oxidation approach, which electrochemically activates graphic carbon layers of CC and preferentially induce the in-situ firm attachment of active Na-containing MnO_2 on CC. The amount of deposited H-MnO_2 could be altered by simply changing the deposition time, ensuring the simplicity and controllability of our method. The resultant fiber-shaped flexible asymmetric supercapacitor device (FASC) based on H-MnO_2/ACC-300 (positive electrode) and reduced carbon cloth (RCC, negative electrode) delivers a high volumetric energy density of $3.82\,mWh/cm^3$ at extended potential window of 4 V. Furthermore, the H-MnO_2/ACC electrodes were systematically investigated in three-electrode cell, delivering superior electrochemical performance.

2. Experimental section

2.1. Preparation of H-MnO₂/ACC

The carbon cloth (WOS1002) was purchased from Cetech Co., Ltd. without any further purification. $Mn(CH_3COO)_2·4H_2O$ (0.4 M) and Na_2SO_4 (0.6 M) were dissolved in distilled water (18.2 MΩ) as a solution for the AED process of H-MnO_2. The AED process of H-MnO_2 was operated on a workstation (CHI660D, Chenhua, Shanghai, China) at room temperature (RT). A piece of carbon cloth ($2 \times 1\,cm^2$, 0.32 mm in thickness) was used as working electrode in a three-electrode configuration at a constant potential of 3 V. Deposition time of 50, 100, 150, 200, 300, 400 and 500 s were applied for each of the carbon cloth. Finally, the H-MnO_2/ACC samples were cleaned with ethanol and water. The H-MnO_2/ACC samples with different deposition time were denoted as H-MnO_2/ACC-50, H-MnO_2/ACC-100, H-MnO_2/ACC-150, H-MnO_2/ACC-200, H-MnO_2/ACC-300, H-MnO_2/ACC-400 and H-MnO_2/ACC-500, respectively. For comparison, MnO_2 was also deposited on CC with a commonly used potential of 1.0 V following similar procedures mentioned above. To study the change of CC after electrodeposition, the electrode was immersed in 6 M HCl to etch the surface layer away.

2.2. Assembly of fiber-shaped asymmetric supercapacitor

Flexible supercapacitors were assembled with as-prepared H-MnO_2/ACC-300 as positive electrode and reduced carbon cloth (RCC) as the negative one, respectively. The 1-ethyl-3-methylimidazolium tetrafluoroborate ($EMIMBF_4$)/tetramethylammonium tetrafluoroborate ($TMABF_4$) ionogel (Lanzhou Kaite Trade Co., Ltd.) as a solid-state electrolyte was filled between two electrodes. RCC negative electrode was fabricated by electrochemical activation of CC in a mixed acid of HNO_3 and H_2SO_4 (V/V = 1:1) using three-electrode system containing CC as work electrode and a platinum sheet as counter electrode and a saturated calomel electrode (SCE) as a reference electrode under a constant voltage of 3 V. Then, RCC was transferred into a Teflon-lined stainless-steel autoclave with 80 mL 0.5% hydrazine hydrate and maintained at 100 °C for 30 min to recover its electrical conductivity. Finally, the as-prepared RCC sample was washed with distilled water and ethanol to remove any impurities. Besides, the $EMIMBF_4$/$TMABF_4$ ionogel electrolyte was prepared as follows. 1 g PVDF-HFP ($Mw = 5 \times 10^5$, Sigma), 0.9 g $EMIMBF_4$ and 0.1 g $TMABF_4$ were dissolved in 6 g N-methyl pyrrolidone (NMP, Adamas) at room temperature for 12 h and a jelly-like solution was formed ionic electrolyte and separator. Prior to assembling, the H-MnO_2/ACC electrode was soaked in the gel solution for 10 min, and then carefully entangled with the RCC electrode. After that, the sample was dried at 65 °C for 24 h to allow electrolyte solidification. Finally, a thin parafilm was wrapped on FASC to ensure the integrity for further testing.

2.3. Materials characterization

Scanning electronic microscope (SEM) and transmission electron microscope (TEM) were conducted on a JEM-7001F and a JEOL-2100, respectively. The crystallographic structures were investigated by a Rigaku Smartlab X-ray diffractometer using Cu Kα radiation. Raman spectra were recorded by a confocal laser inVia Raman microscope (Renishaw, λ_e = 514 nm). Chemical environment was analyzed by X-Ray photoelectron spectroscopy (XPS, ESCALAB 250Xi, Thermal-Fisher). The water contact angle of the samples was measured by optical contact angle measurement system (DSA100S, KRUSS GmbH, Germany). Nitrogen adsorption-desorption measurement was performed using a Quantachrome autosorb automated gas sorption system. Electrochemical properties were conducted with a electrochemical analyzer (CHI660D). Cyclic voltammetry (CV) ranging from 0 to 1 V,
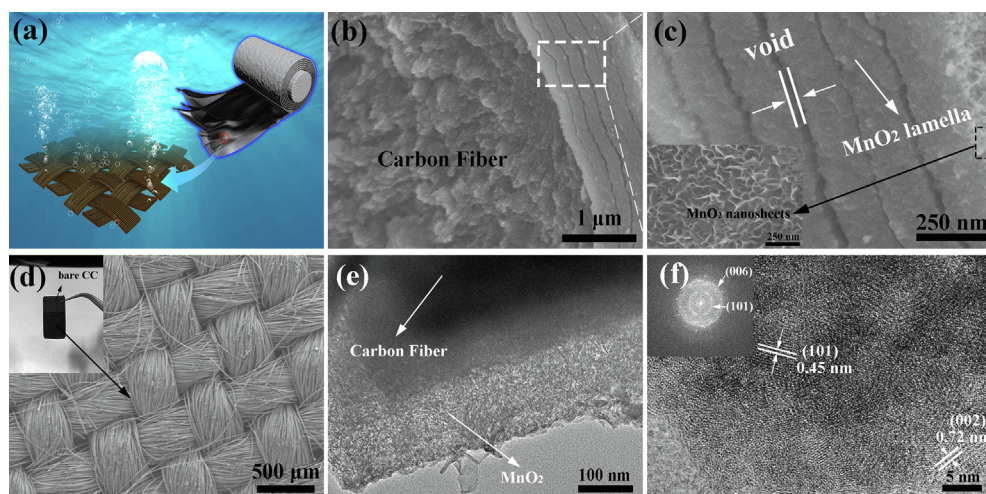
Fig. 1. (a) Schematic representation of the as-prepared electrode. (b) Cross-sectional SEM image of H-MnO$_2$/ACC electro-deposited for 300 s. (c) Magnified SEM image and Top view SEM image of H-MnO$_2$ (the inset). (d) SEM image of H-MnO$_2$/ACC (the inset: photographic image). (e) TEM image of H-MnO$_2$/ACC-300. (f) High-resolution TEM (HRTEM) of H-MnO$_2$, (inset: the corresponding Fast Fourier Transform (FFT) pattern).

galvanostatic charge/discharge (GCD) as well as electrochemical impedance spectroscopy (EIS) of the individual electrode were performed in a three-electrode cell with a Pt counter electrode and a saturated calomel electrode (SCE) reference electrode.

3. Results and discussions

No special equipment or complicated manipulation was required in our method. Activation of CC can be accomplished during the AED process of H-MnO$_2$. During oxidation process, the sulphate ions derived from Na$_2$SO$_4$ are supposed to intercalate into the graphitic regions at the surface of CC and oxidize the nearby carbonaceous structure thereby increasing the electroactive surface area on which further MnO$_2$ can be deposited [33]. Moreover, water is crucial for the overall exfoliation process, as it not only serves as a solvent to decrease the viscosity of the solution, but also produce reactive oxygen-containing species (–COOH, C-OH, etc.) from anodic oxidation, which in turn facilitate the intercalation of SO$_4^{2-}$ [34,35]. The electrolysis of sulfate ions and the co-intercalated water lead to the generation of continuous cavitation bubbles containing SO$_2$, CO, O$_2$ and others (Fig. 1a and Video S1, Supporting Information), all of which will help exfoliate the weakly bonded graphite layers from the defect sites and provide large forces to reduce MnO$_2$ aggregation. In a typical experiment, further applying high overvoltage (η) causes a high nuclei formation rate, as defined by electrochemical version of the Kelvin equation (Eq. (1)):

$$r = \frac{2\sigma V}{ze_0\,|\eta|} \tag{1}$$

where r means the critical nucleation radius, σ is the specific surface energy, V is the atomic volume in the crystal, z is the number of elementary charges (e$_0$). Accordingly, the metal ion concentration in the vicinity of CC decreases drastically and therefore the process becomes diffusion-controlled, which may restrict the continuous crystallite growth of MnO$_2$. To further probe the process, elevated temperature with higher ion mobility is applied, which allows the metal ions to diffuse from the bulk electrolyte to the anode and compensate the metal ion depletion. As expected, we observed the advent of a dense layer of MnO$_2$ at 60 °C. (Fig. S1)

The cross-sectional SEM image (Fig. 1b) reveals that concentric H-MnO$_2$ lamellae with an average thickness of 150 nm are hierarchically deposited and strongly adhered to ACC by applying a high anodic voltage of 3 V at room temperature. Moreover, the exposed part of ACC exhibits a relatively rough surface, indicating the successful activation of carbon fiber surface (inset of Fig. S2b) [19,31]. Significantly, similar morphology can be maintained and the number of MnO$_2$ lamellae can be tailored over a wide range of about 1 to 8 in samples with increasing

deposition time, as depicted in Fig. S2. With the increased magnification, MnO$_2$ lamellae with well-defined neighboring voids form an open framework offering more available active sites for electrolyte intercalating the inner surface (Fig. 1c), which is crucial for the construction of high mass loading electrodes [18,29]. Additionally, the MnO$_2$ nanosheets on the surface of H-MnO$_2$/ACC are interconnected with each other, forming a highly porous surface (inset in Fig. 1c). The porous surface, in combination with the open voids (Fig. S2h), allows better flexibility to buffer the internal strain and offers accessible inner channels for rapid transfer of electrolyte ions [17]. According to Fig. 1d, these CC fibers are intermeshed with each other, forming a three-dimensional (3D) scaffold with a woven fibrous texture. After the AED, the H-MnO$_2$/ACC can be clearly distinguished by their brownish dark color in comparison with the bare parts of the CC (inset in Fig. 1d). The TEM image in Fig. 1e indicates that the entire surface of ACC is completely covered with interconnected crumpled MnO$_2$ nanosheets, well consistent with SEM observations. The HRTEM image of H-MnO$_2$ (Fig. 1f) displays the parallel fringe with a spacing of 0.45 nm for the (1 0 1) plane and 0.72 nm for the (0 0 2) plane, corresponds to hexagonal birnessite-MnO$_2$. The corresponding FFT pattern in inset of Fig. 1f can be further indexed to (1 0 1) and (0 0 6) diffraction planes of the hexagonal MnO$_2$ phase. Besides, EDS analysis (Fig. S3b) unambiguously reconfirms the coaxial H-MnO$_2$/ACC structure and the mapping result is consistent with the EDS spectrum in Fig. S3a, in which a trace of Na element was introduced into the interlayer of MnO$_2$ during the growth [17].

Fig. 2a shows the XRD patterns of H-MnO$_2$/ACC-300 and pristine CC. Two broad peaks centered at 25.4° and 43.5° are attributing to the (0 0 2) and (1 0 1) diffractions from a turbostratic graphitic feature of CC [36,37]. After deposition, three additional diffraction peaks are observed at about 36.9°, 54.4°, and 66.5°, which are indexed to the (0 0 6), (3 0 1), and (1 1 9) crystal faces of hexagonal birnessite-MnO$_2$ without any other impurities (JCPDF 18–0802), respectively [38]. Meanwhile, the low intensity of these peaks suggests that the deposited MnO$_2$ has low crystallinity and fine grain size [28].

Moreover, Raman spectroscopy of the product verifies the existence of MnO$_2$ and successful activation of CC. Three distinct peaks are positioned at 482, 578 and 655 cm^{-1} (Fig. 2b). The pronounced Raman band at 655 cm^{-1} can be ascribed to the Mn-O symmetric stretching vibrations of MnO$_6$ octahedrons, while the characteristic band located at 578 cm^{-1} is usually attributed to the Mn-O stretching vibration in the basal plane of MnO$_6$ sheet [28,39,40]. For bare CC, a disorder-induced D-band peak at 1351 cm^{-1} and a typical sp^2-related G-band peak at 1596 cm^{-1} can be observed, and the relatively low intensity ratio (ca. 0.98) between them indicates that the CC is very clean with high quality. Compared with CC in previously reported findings [41], the
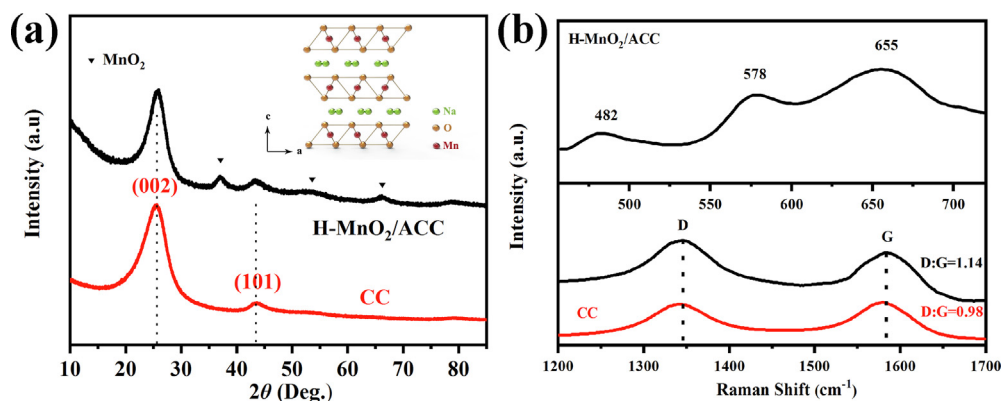
Fig. 2. (a) XRD patterns of the H-MnO$_2$/ACC-300 and pristine CC. (b) Raman spectra of the pristine CC and H-MnO$_2$/ACC-300.
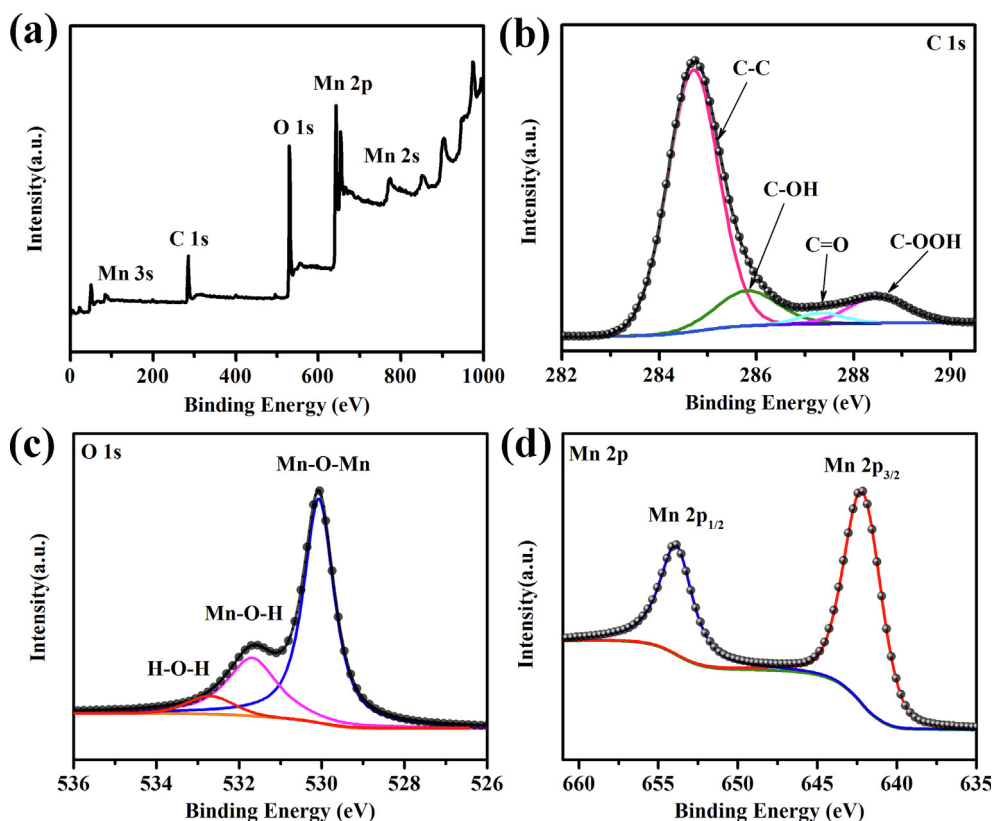

Fig. 3. (a) XPS survey spectrum of the H-MnO$_2$/ACC-300. High-resolution spectra for (b) C 1s, (c) O 1s, and (d) Mn 2p spectra.

increasing of I_D/I_G reveals an intensified degree of disorder, verifying the activation of CC during the AED process.

X-ray photoelectron spectroscopy (XPS) was conducted to further study the chemical composition of H-MnO$_2$/ACC-300. The full spectrum scan is shown in Fig. 3a. It reveals characteristic C, Mn and O peaks in "lamella-void-lamella" H-MnO$_2$/ACC composite, in good agreement with XRD analysis results. By employing a Gaussian fitting approach, the C1s spectrum (Fig. 3b) was deconvoluted into four peaks, which are assigned to C–C (284.7 eV), -C-OH (285.8 eV), C = O (287.3 eV), and –COOH (288.5 eV) groups, confirming the dramatically increased functional groups on ACC surface after anodic oxidation process [42,43]. Based on the analysis of O 1 s spectra (Fig. 3c) [27], the oxidation state can be estimated using Eq. (2):

$$oxidation\ State\ =\ 4 - S_{Mn-OH}/S_{Mn-OH\text{-}Mn} \qquad (2)$$

where S is the peak intensity. The obtained average oxidation state for Mn is 3.6, closer to a 4$^+$ state than a 3$^+$ state. This result is in good

accordance with the XPS results of Mn 3 s spectrum (Fig. S4). Additionally, a spin-energy separation of 11.8 eV between Mn 2p$_{3/2}$ and Mn 2p$_{1/2}$ peaks (Fig. 3d), which can be attributed to MnO$_2$, allows us to further reveal the dominance of Mn 4$^+$ in sample [26,27,44]. Abundant H-O-H groups and co-existence of tetravalent and trivalent oxidation states can dramatically facilitate the electrochemical reactions [26,44]. The nitrogen sorption measurement was carried out to explore porosity (Fig. S4b). The distinct hysteresis loop in the relative pressure range of 0.4–1.0 (inset of Fig. S4b) suggests the presence of an appreciable amount of mesopores (corresponding to a surface area of 81.37 m^2 g^{-1}). The H-MnO$_2$/ACC-300 reveals mesoporous nature with an average pore diameter of 3.41 nm. Such mesoporous nature benefits to the efficient charge transportation, which subsequently results in enhanced electrochemical performance.

The as-synthesized H-MnO$_2$/ACC-300 was assembled into solid-state flexible asymmetric supercapacitors in order to evaluate its electrochemical performance and potential application. Since the energy
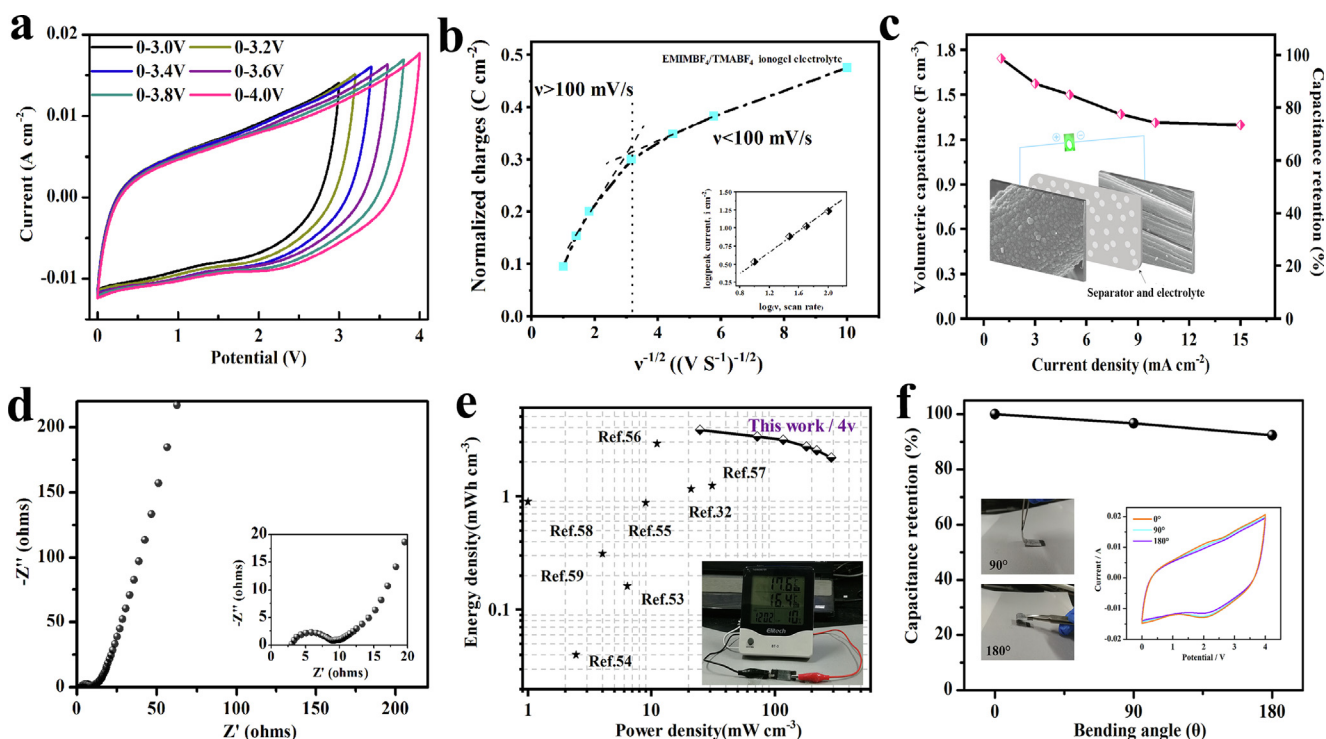
Fig. 4. Capacitive performance of the fabricated flexible supercapacitor (H-MnO$_2$/ACC//RCC). (a) CV curves at different cell voltages with a scan rate of 100 mV/s. (b) The plot of charges versus $v^{-1/2}$ (the inset: log (i) versus log (v) of CV curves from 10 to 100 mV/s). (c) Variations of the capacitance with current densities. (d) Nyquist plots. (e) Ragone plots. The Inset is a digital image of one assembled flexible supercapacitor that is powering an intelligent electronic device. (f) Capacitance retention under different bending angles.

density of SCs highly depends on the square of its voltage, we enlarge the stable electrochemical window to 4 V. To match the capacitance of the H-MnO$_2$/ACC-300 cathode, RCC was fabricated as an anode (Figs. S5, S6a, b). The mixed ionogel (EMIMBF$_4$/TMABF$_4$) was used as a binder, separator, and electrolyte [45]. Because of large viscosity of the ionogel, the two-fiber electrodes can be closely contacted. The H-MnO$_2$/ACC//RCC FASC displays ideal capacitive behavior with quasi-rectangular CV loops, even at a potential window of 4 V (Fig. 4a). Moreover, there is no obvious resistive behavior and the CV profiles still retain rectangular shape at a maximum cell voltage of 4 V at a scan rate as high as 1000 mV/s, suggesting an excellent rate capability without parasitic reactions (Fig. S6c) [46]. It is well-known that pseudocapacitive behavior of MnO$_2$ in aqueous electrolytes is induced by the intercalation/extraction of various cations (K$^+$, Na$^+$, Li$^+$, and H$^+$) or protons (H$_3$O$^+$) [47]. Nevertheless, as proposed in literature [48], BF$_4^-$ anions with smaller size in ionogel electrolyte serve as working species that electro-neutralize the Mn^{3+}/Mn^{4+} redox transition, which reversibly enter/leave the tunnels between MnO$_6$ octahedral units (Eqn. (3)). The multi-cation (TMA$^+$ and EMIM$^+$) species can be packed more densely and adsorbed at the electrode surface, contributing to the overall capacitance.

$$MnO_{2-x}(BF_4^-)_{2x} + 2Xe \leftrightarrow MnO_{2-x} + 2x(BF_4^-) \qquad (3)$$
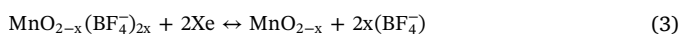
To gain further insight into electrochemical kinetics, the total stored charge (Q) is studied by extrapolating Q versus $v^{-1/2}$. As illustrated in Fig. 4b, two fitted linear plots can be clearly identified on both sides of 100 mV/s (in which $v^{-1/2}$ equal to 3.16). The Q decreases dramatically with respect to the region where the scan rate is higher than 100 mV/s, which arises largely from the irreversible redox transitions of MnO$_2$ and diffusive resistance of electrolyte ions [49,50]. Theoretically, the peak current (i) and scan rate (v) obey a power-law relationship (Eq. (4)) [51].

$$i = av^b \qquad (4)$$

where a and b are adjustable values. The value of b can be determined as the slope of log(v)-log(i) plot, which effectively represents the kinetics of charging and discharging process. Generally, the exponent (b) is between 0.5 (diffusion-controlled storage process) and 1 (surface-controlled charge storage behavior). Fitting to Eq. (4) gives a b value of 0.71 for the H-MnO$_2$/ACC//RCC FASC at scan rates from 10 to 100 mV/s, exhibiting both diffusion-controlled and surface capacitive processes [52]. Furthermore, the contribution of pseudo-capacitance (PC) and electrochemical double layer capacitance (EDLC) can be separated by Trasatti method analysis (Fig. S6d). The pseudocapacitive contribution still dominates at high scan rate of 100 mV/s, evidencing high density of charge adsorption sites provided by sufficient void space of H-MnO$_2$ for the in-depth penetration of electrolyte. Besides exhibiting rectangular voltammograms, the nearly linear variation of GCD curves without obvious IR drop (0.03 V at 1 mA cm^{-2}) is another criterion for judging the capacitive behavior (Fig. S6e). This corroborates the fact that the extended potential window exerts little impact on the efficiency of energy preservation/delivery. Based on the GCD curve (Fig. 4c), the calculated total volumetric capacitance of the H-MnO$_2$/ACC//RCC FASC reaches a maximum of 1.74 F cm^{-3} at a current density of 1 mA cm^{-2}. When the current density changes from 1 to 15 mA cm^{-2}, the device shows a good rate capability with 74.5% of volumetric capacitance retained. The diameter of the semicircle verifies a small value (5.49 Ω) of the charge transfer resistance (R$_{ct}$) for the H-MnO$_2$/ACC//RCC FASC (Fig. 4d). This can be ascribed to the fact that highly conductive paths built through intimately attached interfaces of activated CC and hierarchical MnO$_2$, facilitating electrostatic attraction and ion insertion/extraction. Furthermore, a 45° slopped portion at the intermediate frequency of Nyquist plots, followed by a line almost parallel to Y-axis symbolizing minor Warburg, indicating less obstruction for ion diffusion and a prominent capacitive behavior. Compared with the representatives of the previously reported supercapacitor devices [32,53–59], our device delivers superior volumetric energy density of 3.82 mWh cm^{-3} at a power density of 24.6 mW cm^{-3} and

maintains an energy density of 2.2 mWh cm^{-3} at 285.8 mW cm^{-3} (Fig. 4e). Impressively, one single H-MnO$_2$/ACC//RCC device can successfully drive an electronic device, as presented in the inset of Fig. 4e. After 3200 cycles, approximately 74.3% of the original capacitance is retained with a voltage window of 4 V, which indicates no significant side reactions during GCD cycling (Fig. S7). We then carried out CV measurement at 100 mV/s under different bending states to examine the flexibility and mechanical stability (Fig. 4f). The nearly identical shapes of CV profiles at different bending angles reveal electrical continuity of the FASC in the original and bended state. In addition, small deviations during bending test should be attributed to the movement of contact points and electrodes. After 1000 recycled bending, small cracks could be observed without apparent peeling off of the deposited MnO$_2$ layer, further exhibiting its excellent flexibility (Fig. S8). This is associated with the strengthened interfacial binding force between H-MnO$_2$ and ACC driven by the AED process. The device was also charged to 4 V at a current density of 1 mA cm^{-2} and then recorded the self-discharge with 31.4% retention after 50 h (Fig. S6f). In all, the achievement of high specific capacitance, outstanding rate capability, and wide voltage window pave a way for MnO$_2$-based flexible supercapacitors with high-level energy and power performance.

Usually, the specific capacitance of electrodes with more MnO$_2$ loading is unsatisfactory because of increased electronic resistance between the tight growth sites, prohibiting the reaction between MnO$_2$ and electrolyte [29,60–62]. For comparison, we tested MnO$_2$/CC electrode electrodeposited at common (1 V) and high voltage (3 V). The former takes longer duration (~500 s) to reach the same mass loading of the latter. As expected, the MnO$_2$/CC electrode electrodeposited at high voltage has a higher capacitance, as depicted in Fig. 5a. The GCD curve of the high-voltage sample exhibits only a much smaller IR drop of 0.008 V in comparison to the common-voltage one (0.03 V) from the discharge curve at 1 A/g, indicating its interface enhancement and thus low equivalent series resistance (Fig. 5b). From Fig. 5c, the R$_{ct}$ of the high-voltage sample is almost 10 times less than that of common-

voltage sample, manifests the reduced internal resistance of electrodes and the mitigated ion diffusion resistance at the electrolyte/electrode interface [63,64]. As shown in Fig. S9, we measured the static contact angle of pristine CC and ACC after removing the MnO$_2$ layer. The pristine CC obviously presents an almost unchanged contact angle of ≈118°. After the common-voltage electrodeposition, CC is also hydrophobic with a stable contact angle of 94.6°. In contrast, the ACC after high-voltage electrodeposition reveals its hydrophilic nature with an initial contact angle of 20° and the droplet is absorbed immediately, confirming the activation of CC. These experimental results clearly indicate that conventional ED methods have limitations for improving the electrochemical performance of manganese oxide electrodes with high mass loading. Additionally, hierarchical MnO$_2$, which provide more available active sites for electrolyte penetration, combined with activated carbon cloth is effective to increase capacitance and conductivity. As learnt from above characterizations, very good surface wettability together with such small resistance values also allows enhanced interactions between the electrolyte ions and a rapid ion diffusion channel, which fully contribute to charge storage.

In order to further investigate the influence of MnO$_2$ loading on the electrochemical performance during the anodic oxidation process, the comparative electrochemical studies were conducted for the H-MnO$_2$/ACC electrodes in three-electrode cells containing 1 M Na$_2$SO$_4$ electrolyte. From Fig. 6a, it can be clearly seen that the CV profile of H-MnO$_2$/ACC-100 electrode exhibits the largest enclosed area than the other electrodes, suggestive of its highest capacitance value. Meanwhile, the slight distortion in CV profile of H-MnO$_2$/ACC-50 is caused by the incomplete formation of MnO$_2$ film (inset of Fig. S2a). Areal capacitances of H-MnO$_2$/ACC were collected at different scan rates as a function of mass loading (Fig. 6b). The capacitance portrays an increasing tendency with mass loading (up to 13 mg/cm^2) at scan rates increasing from 5 to 50 mV/s, as expected for a capacitor under the non-diffusion limited conditions [18]. This result reveals most of the active materials participated in charge storage. At high scan rates
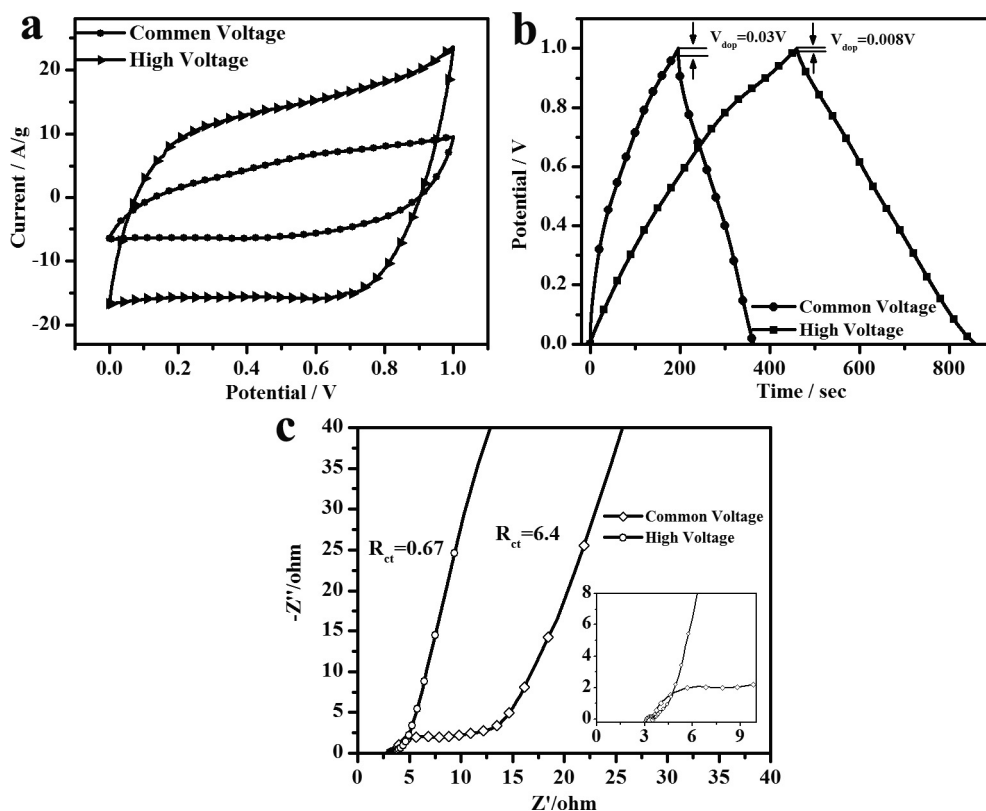

Fig. 5. (a) CV curves, (b) GCD curves, and (c) Nyquist plots for MnO$_2$/CC electrode electrodeposited at common (1 V) and high voltage (3 V).
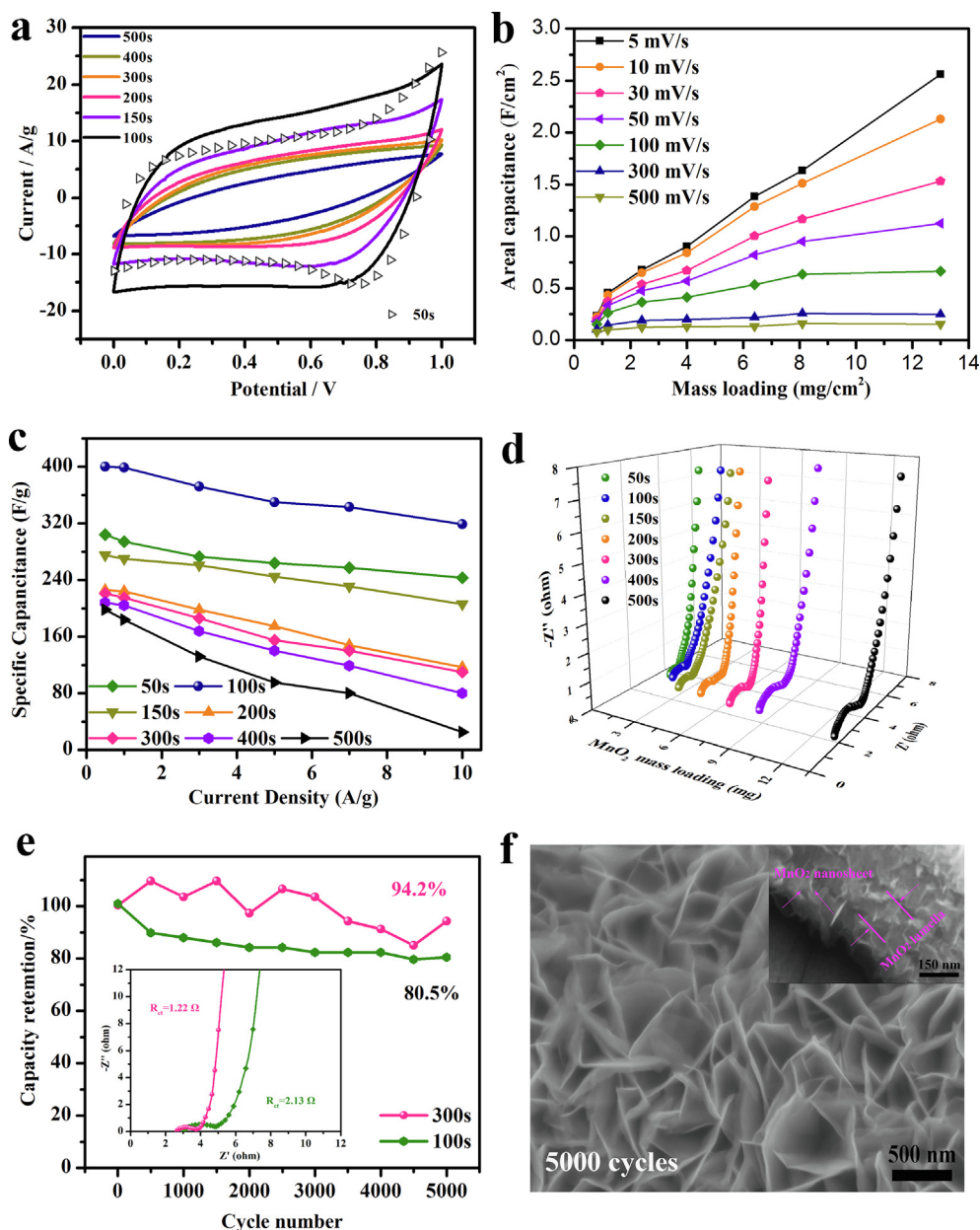
Fig. 6. (a) Comparison of CV curves of H-MnO$_2$/ACC electrodes with different deposition time at 50 mV/s. (b) Calculated areal capacitance of H-MnO$_2$/ACC electrodes with different mass loading (from 0.8 to 13 mg cm^{-2}) at different scan rates from 5 to 500 mV/s. (c) Mass specific capacitance of H-MnO$_2$/ACC collected at different current densities. (d) Nyquist plots of H-MnO$_2$/ACC with different deposition time. (e) Cycling performance of H-MnO$_2$/ACC-100 and H-MnO$_2$/ACC-300 at a current density of 5 A/g for 5000 cycles (the inset shows the corresponding Nyquist plots after 5000 cycles). (f) SEM image of the H-MnO$_2$/ACC-300 electrode after 5000-cycle GCD measurement and the inset is the corresponding cross-sectional SEM images.

beyond 100 mV/s, capacitive saturation can be observed at a high mass loading over 6 mg/cm^2 (related to the H-MnO$_2$/ACC-300 sample), implying that ion penetration might reach a limitation depth [65]. Negligible IR drops (less than 0.01 V) are observed in the GCD profiles of all samples at 1 mA/cm^2 (Fig. S10). The specific capacitance plots based on the GCD curves versus current densities are shown in Fig. 6c. Impressively, the capacitance of H-MnO$_2$/ACC-100 can reach up to 400 F/g at 0.5 A/g, higher than those of recently reported MnO$_2$-based pseudocapacitive materials with a similar or even lower mass loading, such as core–shell-like MnO$_2$@MnO$_2$/carbon cloth (244.54 F/g at 0.5 A/g) [31], Na$_{0.5}$MnO$_2$/carbon cloth (287 F/g at 1 A/g) [17], MnO$_2$/3D duct-like graphene (~255 F/g at 5 mV/s) [66], MnO$_2$ nanoflake/CNTs/Ni (~340 F/g at 1 A/g) [67], MnO$_2$/porous carbon (345.1 F/g at 0.5 A/g) [68], and MnO$_2$ nanorod/carbon fiber paper (362.5 F/g at 0.5 A/g) [69]. Even with a 20 times increment at 10 A/g, superb capacitance retention of 79.7% of the value at 0.5 A/g can still be obtained, showing the exceptional rate capability. Although maximum specific capacitances are close for H-MnO$_2$/ACC electrodes with increased MnO$_2$ loading, the decreased rate performance of H-MnO$_2$/ACC electrode was

achieved after electrodeposited for more than 300 s, indicative of restricted ion penetration into narrow voids. Typically, electrochemically deposited MnO$_2$ film have a dense morphology and increased ion diffusion length as the loading time increases, which might cause diffusion drag of electrolyte ions. The problem may be well-resolved just by integration of hierarchical structure with free void space between neighboring thin films for electrolyte infiltration and ion diffusion without any blocks, which is proved by the electrochemical impedance spectroscopy (EIS). Fig. 6d shows that the R$_{ct}$ only increases slightly when the H-MnO$_2$ loading increases up to about 6 mg/cm^2. While, further increasing the mass loading of MnO$_2$ to 8.1 mg/cm^2, a significant increase of R$_{ct}$ from 1.21 to 1.95 Ω can be obtained, suggesting the blocked ion pathways due to sheets aggregation of thicker MnO$_2$ film. Then, we take representative samples of H-MnO$_2$/ACC-100 and H-MnO$_2$/ACC-300 for further investigation.

Remarkable capacitance retention is a crucial parameter for the practical application of SCs. It is found that the H-MnO$_2$/ACC-100 electrode undergoes a profound loss of 19.5% after 5000 cycles, whereas the H-MnO$_2$/ACC-300 electrode cycles at 5 A/g with a better

capacity retention of 94.2% (Fig. 6e). The comparison of EIS spectra after cycling test is given in the inset of Fig. 6e. The R_{ct} of H-MnO$_2$/ACC-300 remains almost constant after repeated cycles, while the EIS spectrum of H-MnO$_2$/ACC-100 reveals an increased R_{ct} of 2.13 Ω, further validating the prolonged lifetime of H-MnO$_2$/ACC-300 electrode. Furthermore, we measured the microstructure of H-MnO$_2$/ACC-300 after 5000 GCD cycles. A 3D open network is formed by interconnected and larger MnO$_2$ nanosheet arrays on the surface of H-MnO$_2$/ACC-300 (Fig. 6f), which can provide much more accessible area for adsorption of ions. Additionally, the narrow voids also signify its buffering effect to release the internal strain during cycling (inset in Fig. 6f). The observed changes in morphology can be attributed to the dissolution and re-oxidization process of the H-MnO$_2$, which can also facilitate electrolyte transport [70,71]. These results fully illustrate that the presence of hierarchical structure can dramatically enhance utilization efficiency of high mass-loading MnO$_2$, which therefore holds great promise for high performance energy storage devices.

On the basis of the data presented above, we ascribe the ameliorative electrochemical performance of H-MnO$_2$/ACC to the following points: (1) Compared with conventional techniques, our AED yields large amount of well-distributed active materials within exceptionally short time of reaction. Notably, the AED also allows the concentric H-MnO$_2$ fabrication in different precursors (Fig. S11). (2) As particular robust scaffolds, the activated CC electrode contains a high-level of surface oxygen functionalities, which serve as nucleation sites that favor the uniform growth of H-MnO$_2$. (3) The strong attachment of H-MnO$_2$ layers onto ACC reduces the contact resistance at their interface and the hierarchical structure provides in-depth penetration of the electrolyte for available contact with active materials at high rates. A further advantage is that the voids between H-MnO$_2$ lamellae can act as "ion reservoir" to buffer the sharp change of ion concentration during flash charge/discharge processes, which also contributes to excellent rate performance [72].

In summary, the hierarchical concentric H-MnO$_2$ layers were fabricated on carbon cloth via a rapid high-voltage AED process and a perfectly hybridized ACC with tunable number of MnO$_2$ lamellae was obtained. This hierarchical structure ensures good mechanical stability as well as high ionic conductivity. Benefiting from highly conductive paths derived from intimately attached fiber-MnO$_2$ interfaces, hierarchically interpenetrated lamella MnO$_2$ porosity, concentric MnO$_2$ interlayer voids and wide potential window of the EMIMBF$_4$/TMABF$_4$ ionogel electrolyte, the resultant FASC delivers a high volumetric energy density of 3.82 mWh/cm^3. The optimized H-MnO$_2$/ACC-100 electrode exhibits a maximum three-electrode specific capacitance of 400 F/g in 1 M Na$_2$SO$_4$ at 0.5 A/g with excellent rate performance. In addition, the H-MnO$_2$/ACC-300 electrode with high mass loading can retain 94.2% of initial capacitance upon 5000 cycles. We believe that this high-voltage AED process is a general strategy that can be extended to other materials, thus providing new opportunities for improving the performance of high mass loading SC electrodes.

Acknowledgment

Appendix A. Supplementary data

Supplementary data to this article can be found online at https://doi.org/10.1016/j.cej.2019.04.202.

References

[1] Y. Yue, N. Liu, Y. Ma, S. Wang, W. Liu, C. Luo, H. Zhang, F. Cheng, J. Rao, X. Hu, Highly Self-Healable 3D Microsupercapacitor with MXene-Graphene Composite Aerogel, ACS Nano 12 (2018) 4224.

[2] N. Liu, W. Ma, J. Tao, X. Zhang, J. Su, L. Li, C. Yang, Y. Gao, D. Golberg, Y. Bando, Cable-type supercapacitors of three-dimensional cotton thread based multi-grade nanostructures for wearable energy storage, Adv. Mater. 25 (2013) 4925.

[3] T. Li, H. Yu, L. Zhi, W. Zhang, L. Dang, Z. Liu, Z. Lei, Facile electrochemical fabrication of porous Fe$_2$O$_3$ nanosheets for flexible asymmetric supercapacitors, J. Phys. Chem. C 121 (2017) 18982.

[4] L. Zhi, W. Zhang, L. Dang, J. Sun, F. Shi, H. Xu, Z. Liu, Z. Lei, Holey nickel-cobalt layered double hydroxide thin sheets with ultrahigh areal capacitance, J. Power Sources 387 (2018) 108.

[5] J. Tao, N. Liu, J. Rao, L. Ding, M.R.A. Bahrani, L. Li, J. Su, Y. Gao, Series asymmetric supercapacitors based on free-standing inner-connection electrodes for high energy density and high output voltage, Nanoscale 6 (2014) 15073.

[6] W. Liu, N. Liu, Y. Yue, J. Rao, F. Cheng, J. Su, Z. Liu, Y. Gao, Piezoresistive pressure sensor based on synergistical innerconnect polyvinyl alcohol nanowires/wrinkled graphene film, Small 14 (2018) 1704149.

[7] A. Chortos, Z. Bao, Skin-inspired electronic devices, Mater. Today 17 (2014) 321.

[8] J. Tang, M. Jin, P. Yuan, Y. Fu, X. Ma, Large-Area, Ultrathin Inorganic Network Coverages-Graphene Hierarchical Electrodes for Flexible, Heat-Resistant Energy Storage Application, Adv. Energy Mater. 6 (2016) 1600146.

[9] D. Yu, Q. Qian, L. Wei, W. Jiang, K. Goh, J. Wei, J. Zhang, Y. Chen, Emergence of fiber supercapacitors, Chem. Soc. Rev. 44 (2015) 647.

[10] T. Lv, Y. Yao, N. Li, T. Chen, Wearable fiber-shaped energy conversion and storage devices based on aligned carbon nanotubes, Nano Today 11 (2016) 644.

[11] J. Di, X. Zhang, Z. Yong, Y. Zhang, D. Li, R. Li, Q. Li, Carbon-Nanotube Fibers for Wearable Devices and Smart Textiles, Adv. Mater. 28 (2016) 10529.

[12] Z. Yu, L. Tetard, L. Zhai, J. Thomas, Supercapacitor electrode materials: nanostructures from 0 to 3 dimensions, Energy Environ. Sci. 8 (2015) 702.

[13] W. Liu, M.S. Song, B. Kong, Y. Cui, Flexible and stretchable energy storage: recent advances and future perspectives, Adv. Mater. 29 (2017) 1603436.

[14] L. Dong, C. Xu, Y. Li, Z.-H. Huang, F. Kang, Q.-H. Yang, X. Zhao, Flexible electrodes and supercapacitors for wearable energy storage: a review by category, J. Mater. Chem. A 4 (2016) 4659.

[15] X. Lu, M. Yu, G. Wang, Y. Tong, Y. Li, Flexible solid-state supercapacitors: design, fabrication and applications, Energy Environ. Sci. 7 (2014) 2160.

[16] S. Wang, N. Liu, C. Yang, W. Liu, J. Su, L. Li, C. Yang, Y. Gao, Fully screen printed highly conductive electrodes on various flexible substrates for asymmetric supercapacitors, RSC Adv. 5 (2015) 85799.

[17] N. Jabeen, A. Hussain, Q. Xia, S. Sun, J. Zhu, H. Xia, High-Performance 2.6 V Aqueous Asymmetric Supercapacitors based on In Situ Formed Na$_{0.5}$MnO$_2$ Nanosheet Assembled Nanowall Arrays, Adv. Mater. 29 (2017) 1700804.

[18] Y. Song, T. Liu, B. Yao, M. Li, T. Kou, Z.-H. Huang, D.-Y. Feng, F. Wang, Y. Tong, X.-X. Liu, Ostwald ripening improves rate capability of high mass loading manganese oxide for supercapacitors, ACS Energy Lett. 2 (2017) 1752.

[19] S.C. Sekhar, G. Nagaraju, J.S. Yu, Conductive silver nanowires-fenced carbon cloth fibers-supported layered double hydroxide nanosheets as a flexible and binder-free electrode for high-performance asymmetric supercapacitors, Nano Energy 36 (2017) 58.

[20] X.H. Wang, C. Guan, L.M. Sun, R.A. Susantyoko, H.J. Fan, Q. Zhang, Highly stable and flexible Li-ion battery anodes based on TiO$_2$ coated 3D carbon nanostructures, J. Mater. Chem. A 3 (2015) 15394.

[21] Y. Song, T.Y. Liu, B. Yao, T.Y. Kou, D.Y. Feng, X.X. Liu, Y. Li, Amorphous Mixed-Valence Vanadium Oxide/Exfoliated Carbon Cloth Structure Shows a Record High Cycling Stability, Small 13 (2017) 1700067.

[22] X. Zhou, Q. Chen, A. Wang, J. Xu, S. Wu, J. Shen, Bamboo-like composites of V$_2$O$_5$/polyindole and activated carbon cloth as electrodes for all-solid-state flexible asymmetric supercapacitors, ACS Appl. Mater. Interfaces 8 (2016) 3776.

[23] D. Xu, D. Chao, H. Wang, Y. Gong, R. Wang, B. He, X. Hu, H.J. Fan, Flexible Quasi-Solid-State Sodium-Ion Capacitors Developed Using 2D Metal-Organic-Framework Array as Reactor, Adv. Energy Mater. 8 (2018) 1702769.

[24] Y. Wang, Z. Ma, Y. Chen, M. Zou, M. Yousaf, Y. Yang, L. Yang, A. Cao, R.P. Han, Controlled Synthesis of Core-Shell Carbon@ MoS$_2$ Nanotube Sponges as High-Performance Battery Electrodes, Adv. Mater. 28 (2016) 10175.

[25] N. Yu, H. Yin, W. Zhang, Y. Liu, Z. Tang, M.Q. Zhu, High-Performance Fiber-Shaped All-Solid-State Asymmetric Supercapacitors Based on Ultrathin MnO$_2$ Nanosheet/Carbon Fiber Cathodes for Wearable Electronics, Adv. Energy Mater. 6 (2016) 1501458.

[26] L. Yuan, X.-H. Lu, X. Xiao, T. Zhai, J. Dai, F. Zhang, B. Hu, X. Wang, L. Gong, J. Chen, Flexible solid-state supercapacitors based on carbon nanoparticles/MnO$_2$ nanorods hybrid structure, ACS Nano 6 (2011) 656.

[27] M. Toupin, T. Brousse, D. Bélanger, Charge storage mechanism of MnO$_2$ electrode used in aqueous electrochemical capacitor, Chem. Mater. 16 (2004) 3184.

[28] J.-G. Wang, Y. Yang, Z.-H. Huang, F. Kang, Coaxial carbon nanofibers/MnO$_2$ nanocomposites as freestanding electrodes for high-performance electrochemical capacitors, Electrochim. Acta 56 (2011) 9240.

[29] Z.-H. Huang, Y. Song, D.-Y. Feng, Z. Sun, X. Sun, X.-X. Liu, High mass loading MnO$_2$ with hierarchical nanostructures for supercapacitors, ACS Nano 12 (2018) 3557.

[30] T. Zhai, X. Lu, F. Wang, H. Xia, Y. Tong, MnO$_2$ nanomaterials for flexible supercapacitors: performance enhancement via intrinsic and extrinsic modification, Nanoscale Horiz. 1 (2016) 109.

[31] G. Nagaraju, Y.H. Ko, S.M. Cha, S.H. Im, J.S. Yu, A facile one-step approach to

hierarchically assembled core–shell-like $MnO_2@MnO_2$ nanoarchitectures on carbon fibers: an efficient and flexible electrode material to enhance energy storage, Nano Res. 9 (2016) 1507.

[32] Z. Pan, Y. Qiu, J. Yang, F. Ye, Y. Xu, X. Zhang, M. Liu, Y. Zhang, Ultra-endurance flexible all-solid-state asymmetric supercapacitors based on three-dimensionally coated MnO_x nanosheets on nanoporous current collectors, Nano Energy 26 (2016) 610.

[33] Z.Y. Xia, S. Pezzini, E. Treossi, G. Giambastiani, F. Corticelli, V. Morandi, A. Zanelli, V. Bellani, V. Palermo, The exfoliation of graphene in liquids by electrochemical, chemical, and sonication-assisted techniques: A nanoscale study, Adv. Funct. Mater. 23 (2013) 4684.

[34] S. Yang, M.R. Lohe, K. Müllen, X. Feng, New-Generation Graphene from Electrochemical Approaches: Production and Applications, Adv. Mater. 28 (2016) 6213.

[35] K. Parvez, Z.-S. Wu, R. Li, X. Liu, R. Graf, X. Feng, K. Müllen, Exfoliation of graphite into graphene in aqueous solutions of inorganic salts, J. Am. Chem. Soc. 136 (2014) 6083.

[36] X. Ning, W. Zhong, S. Li, Y. Wang, W. Yang, High performance nitrogen-doped porous graphene/carbon frameworks for supercapacitors, J. Mater. Chem. A 2 (2014) 8859.

[37] W. Niu, L. Li, X. Liu, N. Wang, J. Liu, W. Zhou, Z. Tang, S. Chen, Mesoporous N-doped carbons prepared with thermally removable nanoparticle templates: an efficient electrocatalyst for oxygen reduction reaction, J. Am. Chem. Soc. 137 (2015) 5555.

[38] M.N. Patel, X. Wang, B. Wilson, D.A. Ferrer, S. Dai, K.J. Stevenson, K.P. Johnston, Hybrid MnO_2-disordered mesoporous carbon nanocomposites: synthesis and characterization as electrochemical pseudocapacitor electrodes, J. Mater. Chem. 20 (2010) 390.

[39] G. Yu, L. Hu, N. Liu, H. Wang, M. Vosgueritchian, Y. Yang, Y. Cui, Z. Bao, Enhancing the supercapacitor performance of graphene/MnO_2 nanostructured electrodes by conductive wrapping, Nano Lett. 11 (2011) 4438.

[40] C. Julien, M. Massot, R. Baddour-Hadjean, S. Franger, S. Bach, J. Pereira-Ramos, Raman spectra of birnessite manganese dioxides, Solid State Ionics 159 (2003) 345.

[41] Y. Zhang, Z. Hu, Y. An, B. Guo, N. An, Y. Liang, H. Wu, High-performance symmetric supercapacitor based on manganese oxyhydroxide nanosheets on carbon cloth as binder-free electrodes, J. Power Sources 311 (2016) 121.

[42] C.-Y. Su, A.-Y. Lu, Y. Xu, F.-R. Chen, A.N. Khlobystov, L.-J. Li, High-quality thin graphene films from fast electrochemical exfoliation, ACS Nano 5 (2011) 2332.

[43] Q. Gao, L. Demarconnay, E. Raymundo-Piñero, F. Béguin, Exploring the large voltage range of carbon/carbon supercapacitors in aqueous lithium sulfate electrolyte, Energy Environ. Sci. 5 (2012) 9611.

[44] D. Yu, K. Goh, Q. Zhang, L. Wei, H. Wang, W. Jiang, Y. Chen, Controlled Functionalization of Carbonaceous Fibers for Asymmetric Solid-State Micro-Supercapacitors with High Volumetric Energy Density, Adv. Mater. 26 (2014) 6790.

[45] N. Chen, H. Zhang, L. Li, R. Chen, S. Guo, Ionogel electrolytes for high-performance lithium batteries: a review, Adv. Energy Mater. 8 (2018) 1702675.

[46] P. Simon, Y. Gogotsi, Capacitive energy storage in nanostructured carbon-electrolyte systems, Acc. Chem. Res. 46 (2012) 1094.

[47] W. Wei, X. Cui, W. Chen, D.G. Ivey, Manganese oxide-based materials as electrochemical supercapacitor electrodes, Chem. Soc. Rev. 40 (2011) 1697.

[48] J.-K. Chang, M.-T. Lee, W.-T. Tsai, M.-J. Deng, I.-W. Sun, X-ray photoelectron spectroscopy and in situ X-ray absorption spectroscopy studies on reversible insertion/desertion of dicyanamide anions into/from manganese oxide in ionic liquid, Chem. Mater. 21 (2009) 2688.

[49] C. De Pauli, S. Trasatti, Electrochemical surface characterization of IrO_2^+ SnO_2 mixed oxide electrocatalysts, J. Electroanal. Chem. 396 (1995) 161.

[50] Q. Xue, H. Gan, Y. Huang, M. Zhu, Z. Pei, H. Li, S. Deng, F. Liu, C. Zhi, Boron Element Nanowires Electrode for Supercapacitors, Adv. Energy Mater. (2018) 1703117.

[51] H. Lindström, S. Södergren, A. Solbrand, H. Rensmo, J. Hjelm, A. Hagfeldt, S.-E. Lindquist, Li+ ion insertion in TiO_2 (Anatase). 2. Voltammetry on nanoporous films, J. Phys. Chem. B 101 (1997) 7717.

[52] T. Brezesinski, J. Wang, S.H. Tolbert, B. Dunn, Ordered mesoporous α-MoO_3 with iso-oriented nanocrystalline walls for thin-film pseudocapacitors, Nat. Mater. 9 (2010) 146.

[53] S. Cho, B. Patil, S. Yu, S. Ahn, J. Hwang, C. Park, K. Do, H. Ahn, Flexible, Swiss roll, fiber-shaped, asymmetric supercapacitor using MnO_2 and Fe_2O_3 on carbon fibers, Electrochim. Acta 269 (2018) 499.

[54] P. Yang, X. Xiao, Y. Li, Y. Ding, P. Qiang, X. Tan, W. Mai, Z. Lin, W. Wu, T. Li, Hydrogenated ZnO core–shell nanocables for flexible supercapacitors and self-powered systems, ACS Nano 7 (2013) 2617.

[55] T. Zhai, X. Lu, Y. Ling, M. Yu, G. Wang, T. Liu, C. Liang, Y. Tong, Y. Li, A New Benchmark Capacitance for Supercapacitor Anodes by Mixed-Valence Sulfur-Doped V_6O_{13-x}, Adv. Mater. 26 (2014) 5869.

[56] G. Yang, X.-X. Liu, Electrochemical fabrication of interconnected tungsten bronze nanosheets for high performance supercapacitor, J. Power Sources 383 (2018) 17.

[57] C. Xu, Z.H. Li, C. Yang, P.C. Zou, B.H. Xie, Z.Y. Lin, Z.X. Zhang, B.H. Li, F.Y. Kang, C.P. Wong, An Ultralong, Highly Oriented Nickel-Nanowire-Array Electrode Scaffold for High-Performance Compressible Pseudocapacitors, Adv. Mater. 28 (2016) 4105.

[58] Q.Q. Tang, M.M. Chen, C.Y. Yang, W.Q. Wang, H. Bao, G.C. Wang, Enhancing the Energy Density of Asymmetric Stretchable Supercapacitor Based on Wrinkled $CNT@MnO_2$ Cathode and CNT@polypyrrole Anode, ACS Appl. Mater. Interfaces 7 (2015) 15303.

[59] Y.X. Zeng, Y. Han, Y.T. Zhao, Y. Zeng, M.H. Yu, Y.J. Liu, H.L. Tang, Y.X. Tong, X.H. Lu, Advanced Ti-Doped $Fe_2O_3@PEDOT$ Core/Shell Anode for High-Energy Asymmetric Supercapacitors, Adv. Energy Mater. 5 (2015) 7.

[60] Q. Lv, S. Wang, H. Sun, J. Luo, J. Xiao, J. Xiao, F. Xiao, S. Wang, Solid-state thin-film supercapacitors with ultrafast charge/discharge based on N-doped-carbon-tubes/Au-nanoparticles-doped-MnO_2 nanocomposites, Nano Lett. 16 (2015) 40.

[61] W. Tian, X. Mao, P. Brown, G.C. Rutledge, T.A. Hatton, Electrochemically nanostructured polyvinylferrocene/polypyrrole hybrids with synergy for energy storage, Adv. Funct. Mater. 25 (2015) 4803.

[62] J.-H. Kim, K.H. Lee, L.J. Overzet, G.S. Lee, Synthesis and electrochemical properties of spin-capable carbon nanotube sheet/MnO_x composites for high-performance energy storage devices, Nano Lett. 11 (2011) 2611.

[63] L.L. Zhang, X. Zhao, Carbon-based materials as supercapacitor electrodes, Chem. Soc. Rev. 38 (2009) 2520.

[64] C. Li, X. Zhang, K. Wang, X. Sun, G. Liu, J. Li, H. Tian, J. Li, Y. Ma, Scalable Self-Propagating High-Temperature Synthesis of Graphene for Supercapacitors with Superior Power Density and Cyclic Stability, Adv. Mater. 29 (2017) 1604690.

[65] H. Sun, L. Mei, J. Liang, Z. Zhao, C. Lee, H. Fei, M. Ding, J. Lau, M. Li, C. Wang, Three-dimensional holey-graphene/niobia composite architectures for ultrahigh-rate energy storage, Science 356 (2017) 599.

[66] K. Qin, E. Liu, J. Li, J. Kang, C. Shi, C. He, F. He, N. Zhao, Free-Standing 3D Nanoporous Duct-Like and Hierarchical Nanoporous Graphene Films for Micron-Level Flexible Solid-State Asymmetric Supercapacitors, Adv. Energy Mater. 6 (2016) 1600755.

[67] P. Sun, H. Yi, T. Peng, Y. Jing, R. Wang, H. Wang, X. Wang, Ultrathin MnO_2 nanoflakes deposited on carbon nanotube networks for symmetrical supercapacitors with enhanced performance, J. Power Sources 341 (2017) 27.

[68] X. Wang, S. Chen, D. Li, S. Sun, Z. Peng, S. Komarneni, D. Yang, Direct interfacial growth of MnO_2 nanostructure on hierarchically porous carbon for high-performance asymmetric supercapacitors, ACS Sustainable Chem. Eng. 6 (2017) 633.

[69] Z. Ye, T. Li, G. Ma, X. Peng, J. Zhao, Morphology controlled MnO_2 electrodeposited on carbon fiber paper for high-performance supercapacitors, J. Power Sources 351 (2017) 51.

[70] Z. Qiao, X. Yang, S. Yang, L. Zhang, B. Cao, 3D hierarchical MnO_2 nanorod/welded Ag-nanowire-network composites for high-performance supercapacitor electrodes, Chem. Commun. 52 (2016) 7998.

[71] W. Wei, X. Cui, W. Chen, D.G. Ivey, Electrochemical cyclability mechanism for MnO_2 electrodes utilized as electrochemical supercapacitors, J. Power Sources 186 (2009) 543.

[72] Y. Xu, Z. Lin, X. Huang, Y. Wang, Y. Huang, X. Duan, Functionalized graphene hydrogel-based high-performance supercapacitors, Adv. Mater. 25 (2013) 5779.